Original Article | Neuroimaging and Head & Neck

eISSN 2005-8330
https://doi.org/10.3348/kjr.2025.1969
Korean J Radiol 2026;27(7):670-681

Check for updates

Korean Journal of Radiology
KJR

Distinguishing Molecular and Histologic Glioblastomas Using Multiparametric MRI-Based Habitat Analysis

Minseo Choi[1*], Yunseo Choi[2*], Junhyeok Lee[3], Seong Yun Jeong[1], Minchul Kim[4], Inpyeong Hwang[1], Ji Eun Park[5], Yae Won Park[6], Seung Hong Choi[1,7], Kyu Sung Choi[1,7,8]

[1]Department of Radiology, Seoul National University Hospital, Seoul, Republic of Korea
[2]CHA Bundang Medical Center, Seongnam, Republic of Korea
[3]Interdisciplinary Program in Cancer Biology, Seoul National University College of Medicine, Seoul, Republic of Korea
[4]Department of Radiology, Kangbuk Samsung Hospital, Sungkyunkwan University School of Medicine, Seoul, Republic of Korea
[5]Division of Neuroradiology, Russell H. Morgan Department of Radiology and Radiological Science, Johns Hopkins University School of Medicine, Baltimore, MD, USA
[6]Department of Radiology and Research Institute of Radiological Science and Center for Clinical Imaging Data Science, Yonsei University College of Medicine, Seoul, Republic of Korea
[7]Department of Radiology, Seoul National University College of Medicine, Seoul, Republic of Korea
[8]Healthcare AI Research Institute, Seoul National University Hospital, Seoul, Republic of Korea

Objective: To explore how molecular glioblastoma (mol-GBM) differs from histological glioblastoma (hist-GBM) in tumor heterogeneity using multi-parametric physiologic MRI-based tumor habitat analysis.

Materials and Methods: In this multi-institutional retrospective study, imaging data were collected from two tertiary centers: 13 mol-GBMs and 39 hist-GBMs from institution 1 (2007–2024) for habitat definition, model development, and internal validation and nine mol-GBMs were obtained from institution 2 (2020–2024) for external validation. The apparent diffusion coefficient (ADC; cellularity), relative cerebral blood volume (rCBV; vascularity), and volume transfer constant (K^{trans}; permeability) were binarized into high/low categories, which yielded eight spatial habitat clusters to visualize tumor heterogeneity. Habitat proportions and intratumoral heterogeneity features were compared between groups. Multivariable logistic regression models incorporating habitat-derived features were developed to distinguish mol-GBM from hist-GBM, and their performance was evaluated.

Results: Fifty-two patients (hist-GBM, n = 39; mol-GBM, n = 13; mean age, 60.0 ± 11.1 years; 22 male) were evaluated. Habitat analysis revealed that mol-GBM had a significantly lower proportion of the most malignant habitat (cluster 3: low-ADC, high rCBV, high K^{trans}; 0.80% vs. 7.0%, $P < 0.001$). The total proportion of high K^{trans} habitats was markedly lower in the mol-GBM group (5.7% vs. 21.3%, $P < 0.001$). A habitat-based multivariable model incorporating tumor volume, cluster 3 proportion, high K^{trans} proportion, and Shannon entropy achieved an area under receiver operating characteristic curve (AUC) of 0.87 (95% confidence interval [CI]: 0.73–0.97) at internal validation using a leave-one-out cross-validation, which was substantially greater, albeit nonsignificant, than the AUC for tumor size alone (0.70, 95% CI: 0.51–0.85, $P = 0.057$), with an external validation accuracy of 88.9% (8/9).

Conclusion: Multiparametric physiologic MRI habitat analysis demonstrated differences in the tumor heterogeneity between mol-GBM and hist-GBM. Tumor permeability (K^{trans}) was the most discriminating parameter. Incorporating habitat-derived features alongside tumor volume may improve the discrimination of the two subtypes on MRI analysis. Further studies, including more rigorous external validation, are warranted.

Keywords: Glioblastoma; Molecular glioblastoma; Tumor habitat; Diffusion MRI; Perfusion MRI

Received: December 30, 2025 **Revised:** April 24, 2026 **Accepted:** April 26, 2026

*These authors contributed equally to this work.

Corresponding author: Kyu Sung Choi, MD, PhD, Department of Radiology, Seoul National University Hospital, Seoul National University College of Medicine, 101 Daehak-ro, Jongno-gu, Seoul 03080, Republic of Korea
• E-mail: kyuchoi86@gmail.com

This is an Open Access article distributed under the terms of the Creative Commons Attribution Non-Commercial License (https://creativecommons.org/licenses/by-nc/4.0) which permits unrestricted non-commercial use, distribution, and reproduction in any medium, provided the original work is properly cited.

Copyright © 2026 The Korean Society of Radiology

Korean Journal of Radiology
KJR

INTRODUCTION

The 2021 WHO classification of tumors of the central nervous system reclassified histologically low-grade, IDH-wildtype diffuse astrocytoma (WHO grades 2–3) harboring specific molecular alterations (*TERT* promoter mutation, *EGFR* amplification, or chromosome 7 gain/10 loss) as molecular glioblastoma (mol-GBM), WHO grade 4 [1,2]. While hist-GBM is notoriously aggressive [3], mol-GBM demonstrates a similarly poor prognosis [4]. However, longer progression-free survival has been reported for mol-GBM, which may represent an early infiltrative stage of GBM progression [4,5].

Currently, the most established finding is that mol-GBMs demonstrate contrast enhancement less frequently than hist-GBMs [5-7]. Nevertheless, a recent study reported that among non-enhancing IDH-wildtype GBMs, 45% were hist-GBM and 55% were mol-GBM [8], underscoring the need for advanced MRI to distinguish the two types, given the limitations of conventional imaging.

Physiologic MRI, including diffusion-weighted imaging (DWI), dynamic susceptibility contrast (DSC) perfusion imaging, and dynamic contrast-enhanced (DCE) MRI, provides quantitative insight into tumor cellularity, vascularity, and permeability [9-11]. Because mol-GBM lacks pseudopalisading necrosis or microvascular proliferation, these sequences may provide insights into microstructural and vascular heterogeneity that differ between mol-GBM and hist-GBM. Such heterogeneity is associated with biological aggressiveness [12] and can be quantified using the apparent diffusion coefficient (ADC; cellularity), relative cerebral blood volume (rCBV; vascularity), and volume transfer constant (K^{trans}; permeability). Previous studies have shown the value of these physiologic MRI parameters in characterizing the biological behavior of GBM [13-17]. Moreover, tumor habitats based on ADC and rCBV have stratified IDH-wildtype GBMs into prognostic subgroups [17-19], highlighting the value of physiologic MRI parameters in noninvasive prediction of outcomes.

This study evaluated physiologic MRI differences between mol-GBM and hist-GBM. To further explore these differences, ADC, rCBV, and K^{trans} parameters were integrated and a higher-dimensional habitat analysis was performed to visualize and quantify tumor heterogeneity. This multiparametric approach aimed to provide a deeper radiologic insight into mol-GBM.

MATERIALS AND METHODS

Study Population

This retrospective study was approved by the Institutional Review Board of institution 1 (internal dataset, IRB No. 2212-077-1385) and institution 2 (external dataset IRB No. 2023-0525) with a waiver of informed consent. Between November 2007 and October 2024, 689 patients with IDH-wildtype GBM (2021 WHO criteria) were identified at institution 1.

The eligible patients were adults (≥18 years) who had undergone conventional and advanced MRI (DWI, DSC, and DCE). Patients were classified according to the 2021 WHO criteria into hist-GBM, defined as an IDH-wildtype diffuse glioma with microvascular proliferation and/or intratumoral necrosis, and mol-GBM, defined as a histological grade 2–3 IDH-wildtype diffuse glioma carrying the *TERT* promoter mutation, *EGFR* amplification, or +7/-10 chromosome variations. Patients with incomplete MRI or MRI acquired more than 6 months before surgery were excluded. After applying the exclusion criteria, 13 patients with mol-GBM and 476 with hist-GBM were identified. Following 1:3 propensity score matching by age and sex, 52 patients (13 mol-GBM, 39 hist-GBM) were included.

For the external dataset, 18 patients from institution 2 enrolled between February 2020 and February 2024 met identical inclusion criteria, producing 9 mol-GBM (mol-GBM [ext]). The patient enrollment flowchart is shown in Figure 1.

The internal dataset of institution 1 (n = 52) was used for habitat definition, model development, and internal validation. The external dataset of institution 2 (n = 9, all mol-GBM) was used for the independent evaluation.

MRI Acquisitions

For institution 1, MRI studies of all patients were performed using 3T MRI units (Magnetom Verio or Magnetom Skyra; Siemens Healthineers, Erlangen, Germany) with a 32-channel head coil. The MRI protocol included T2-weighted imaging (T2WI), T2 fluid-attenuated inversion recovery (FLAIR), T1-weighted imaging (T1WI), DWI, DCE-MRI, and DSC-MRI, and contrast enhanced (CE) T1WI. For institution 2, the MRI scan was acquired using a 3T MRI unit (Ingenia 3.0 CX, Philips Healthcare, Amsterdam, the Netherlands) including the same sequences applied in institution 1. The detailed MRI acquisition parameters are shown in the Supplement (Magnetic Resonance Imaging Acquisition).

https://doi.org/10.3348/kjr.2025.1969

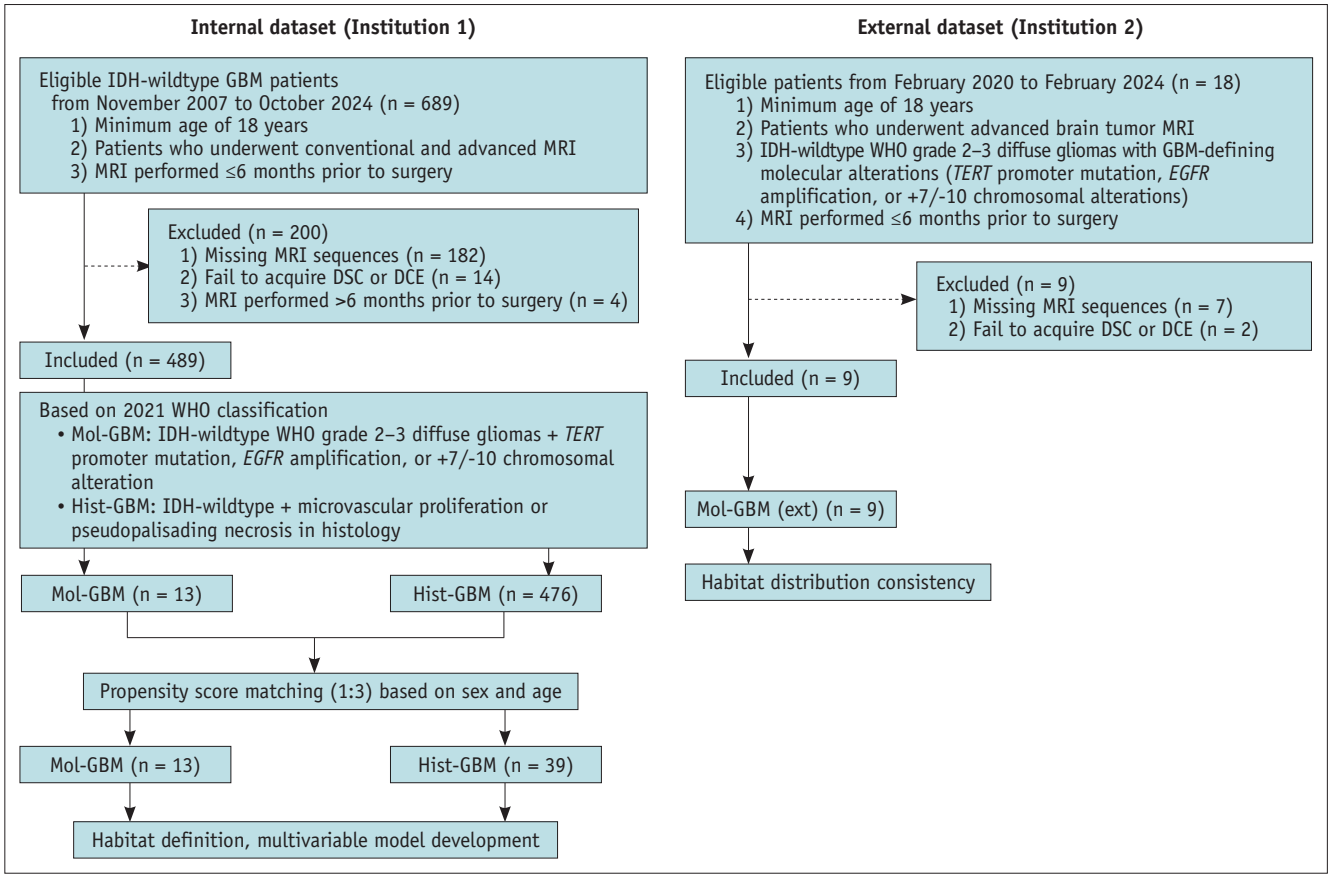

Fig. 1. Flow diagram of the patient selection process. IDH = isocitrate dehydrogenase, GBM = glioblastoma, TERT = telomerase reverse transcriptase, EGFR = epidermal growth factor receptor, DSC = dynamic susceptibility contrast, DCE = dynamic contrast-enhanced, Mol-GBM = molecular glioblastoma, Hist-GBM = histological glioblastoma, Mol-GBM (ext) = molecular glioblastoma from the external dataset

Image Processing

The three-dimensional (3D) CE-T1WI of each patient were resampled to 1 mm isometric voxels. Skull stripping was performed on all MRI sequences using the SynthStrip algorithm [20]. The skull-stripped CE-T1WI served as the reference image, and all other modalities (T2WI, FLAIR, DWI, DSC, and DCE) were co-registered using rigid transformations with the Advanced Normalization Tools [21]. After registration, tumor masks were generated using HD-GLIO [22], and refined by an experienced neuroradiologist (K.S.C, 7 years) and a well-trained research assistant (10 years).

To mitigate inter-institutional batch effects, the ADC, rCBV, and K^{trans} values were normalized using normal white matter reference distributions. The ADC map was calculated using b values of 0 and 1,000 s/mm^2, based on a two-point estimate of signal decay. For DSC and DCE analyses, the pharmacokinetic map calculations were performed using commercial software (Nordic ICE, v4.1.2; Nordic-NeuroLab, Bergen, Norway). For the DSC analysis, the rCBV map was obtained using the Weisskoff–Boxerman method for leakage correction [23]. For DCE analysis, the K^{trans} was calculated using the two-compartment pharmacokinetic model (Extended Tofts Model, eTofts) [24]. Conventional histogram features of ADC, rCBV, and K^{trans} were extracted. Further details are provided in the Supplement (Parametric Mapping for Advanced Image, Batch Effect Correction, Histogram-Based Analysis, and Supplementary Fig. 1).

Multiparametric Physiologic MRI-Based Tumor Habitats

Tumor habitats were defined using voxel-wise ADC, rCBV, and K^{trans} values. For each parameter, Gaussian mixture modeling was applied to derive a single threshold, dichotomizing values into low and high categories. Based on the resulting 2 x 2 x 2 combination, each voxel was classified into one of eight physiologic habitats (e.g., cluster 3: low ADC, high rCBV, high K^{trans}), each representing a distinct tumor microenvironment. Habitat definitions were fixed using the internal dataset and were applied consistently in all subsequent analyses.

https://doi.org/10.3348/kjr.2025.1969

Korean Journal of Radiology
KJR

For each tumor, the proportion of the eight habitat clusters was calculated relative to the total tumor volume. The overall tumor size was represented by log-transformed total tumor volume. Clusters were also grouped by shared physiologic trait, all clusters with high K^{trans} (clusters 1, 3, 5, 7), high rCBV (clusters 2, 3, 6, 7), or low ADC (clusters 0, 1, 2, 3). Cluster 3 (low ADC, high rCBV, high K^{trans}) was prespecified as a marker of the most malignant-appearing tumor habitat.

Intratumoral heterogeneity was quantified using Shannon entropy, the Simpson diversity index, and Pielou evenness derived from the habitat proportions of the eight habitat clusters. The external cohort, consisting exclusively of mol-GBM cases, was used to assess the consistency of the habitat distribution patterns.

Model Development and Validation

Multivariable logistic regression models were developed using the internal cohort (institution 1; n = 52). Features were standardized according to the z-score using the parameters of the internal cohort and were applied identically to the external cohort.

Univariable and multivariable logistic regression analysis was performed to evaluate the association between habitat-derived features and GBM subtypes (mol-GBM vs. hist-GBM). Univariable analysis included all prespecified habitat-derived features: individual cluster proportions, composite habitat proportions (high K^{trans}, high rCBV, and low ADC), Shannon entropy, and log-transformed tumor volume. Variables for the multivariable analysis were selected a priori based on biological relevance and univariable significance, without stepwise selection. As a result, three logistic regression models were defined using variables selected for multivariable modeling to assess the added discriminatory value of habitat-derived features beyond tumor volume. Model V incorporated log-transformed tumor volume only, serving as a clinically accessible reference. Model H added the cluster 3 proportion and the high K^{trans} proportion, selected based on their biological relevance as markers of the malignant microenvironment and the overall permeability burden, respectively. Model H+ further incorporated Shannon entropy to evaluate the incremental value of intratumoral heterogeneity. All models were configured to predict hist-GBM. Further details are provided in the Supplement (Univariable Logistic Regression Analysis and Multivariable Logistic Regression Analysis).

Internal validation was performed using leave-one-out cross-validation (LOOCV) within the internal cohort (n = 52). For each fold, the z-score normalization and an L2-regularized logistic regression (C = 1.0) were fit to the n - 1 training subjects and were applied to the held-out subject. The 52 aggregated out-of-fold probabilities were used to construct receiver operating characteristic (ROC) curves, compute area under the curve (AUC) values, and (95% confidence intervals [CIs] by 1,000-iteration bootstrap), and to define a Youden index-derived threshold, which was held fixed for all subsequent evaluations. After LOOCV, each model was refit on the full internal dataset for external evaluation; this step did not contribute to internal validation metrics. The fixed coefficients were applied to the external cohort using the same threshold. Further details are provided in the Supplement (Model Validation).

Other Statistical Analyses

Patient characteristics were compared between hist-GBM and mol-GBM in the internal dataset, and between internal mol-GBM and mol-GBM (ext), using the independent *t*-test or Mann–Whitney U test for continuous variables, depending on the normality of distribution assessed by the Shapiro–Wilk test, and the chi-squared test for categorical variables. Differences in voxel-wise habitat distributions were analyzed by pairwise permutational multivariate analysis of variance (PERMANOVA) with post-hoc Mann–Whitney U tests. The DeLong test was used for ROC AUC comparison. No formal adjustment for multiple comparisons was applied. A two-sided *P*-value <0.05 was considered statistically significant. Statistical analyses were performed using Python (version 3.10.13; Python Software Foundation, Wilmington, DE, USA) with the SciPy (version 1.15.3), scikit-learn (version 1.7.0), Matplotlib (version 3.10.3), and Seaborn (version 0.13.2) libraries. Propensity score matching was conducted using R (version 3.4.0; R Foundation for Statistical Computing, Vienna, Austria).

RESULTS

Patient Characteristics

The baseline characteristics of the patients are summarized in Table 1. Age and sex did not differ between hist-GBM and mol-GBM subtypes nor between the internal and external mol-GBM cohorts.

Among the mol-GBM group (n = 13), eight patients harbored a *TERT* promoter mutation (8/13, 61.5%), seven patients *EGFR* amplification (7/13, 53.8%), and one patient

 https://doi.org/10.3348/kjr.2025.1969

Table 1. Baseline characteristics of the internal and external dataset

Characteristics	Internal dataset		External dataset	*P**	*P*†
	Hist-GBM (n = 39)	Mol-GBM (n = 13)	Mol-GBM (ext) (n = 9)		
Age at diagnosis, yrs	59.6 ± 11.6	61.1 ± 10.0	64.6 ± 10.9	0.683	0.453
Sex				0.746	1.000
Male	17 (43.6)	5 (38.5)	4 (44.4)		
Female	22 (56.4)	8 (61.5)	5 (55.6)		
Baseline KPS	82.6 ± 11.6	86.7 ± 13.7	95.0 ± 7.6	0.234	0.163
WHO grade				<0.001	0.178
Grade 2	0 (0)	2 (15.4)	4 (44.4)		
Grade 3	0 (0)	11 (84.6)	5 (55.6)		
Grade 4	39 (100)	0 (0)	0 (0)		
Period between MRI and biopsy/surgery, day	3.7 ± 10.2	14.2 ± 32.3	33.1 ± 27.1	0.239	0.004
Contrast Enhancement on T1				<0.001	1.000
No	2 (2.6)	9 (69.2)	6 (66.7)		
Yes	37 (94.9)	4 (30.8)	3 (33.3)		
Tumor volumes, mm^3	76,148 [74,763]	38,843 [27,009]	29,026 [18,674]	0.009	0.229
IDH-wildtype	39 (100)	13 (100)	9 (100)	-	-
TERT promoter mutation				0.034	0.206
No	11 (28.2)	0 (0)	3 (33.3)		
Yes	15 (38.5)	8 (61.5)	6 (66.7)		
NA	13 (33.3)	5 (38.5)	0 (0)		
EGFR amplification				0.164	0.017
No	9 (23.1)	6 (46.2)	9 (100)		
Yes	29 (74.4)	7 (53.8)	0 (0)		
NA	1 (2.5)	0 (0)	0 (0)		
+7/-10 chromosome variations				1.000	0.080
No	20 (51.3)	5 (38.5)	1 (11.1)		
Yes	5 (12.8)	1 (7.7)	5 (55.6)		
NA	14 (35.9)	7 (53.8)	3 (33.3)		
PTEN mutation				0.589	0.494
No	36 (92.3)	11 (84.6)	9 (100)		
Yes	3 (7.7)	2 (15.4)	0 (0)		
MGMT methylation				0.502	0.164
No	24 (61.5)	10 (76.9)	3 (33.3)		
Yes	14 (35.9)	3 (23.1)	5 (55.6)		
NA	1 (2.5)	0 (0)	1 (11.1)		
Ki-67, %	38.3 ± 21.0	14.8 ± 13.0	NA	<0.001	-

Data are presented as mean ± standard deviation, median [interquartile range], and number (%).
**P*-values for pairwise comparison between Mol-GBM and Hist-GBM, †*P*-values for pairwise comparison between Mol-GBM and Mol-GBM (ext). Mol-GBM = molecular glioblastoma, Hist-GBM = histological glioblastoma, Mol-GBM (ext) = molecular glioblastoma from the external dataset, KPS = Karnofsky performance score, IDH = isocitrate dehydrogenase, TERT = telomerase reverse transcriptase, EGFR = epidermal growth factor receptor, +7/−10 = gain of chromosome 7 and loss of chromosome 10, PTEN = phosphatase and tensin homolog, MGMT = O6-methylguanine-DNA methyltransferase, NA = not available, - = not applicable

+7/-10 chromosome variations (1/13, 7.7%). For the mol-GBM (ext) group (n = 9), six patients had *TERT* promoter mutation (6/9, 66.7%) and five patients had +7/-10 chromosome variations (5/9, 55.6%).

Tumor Habitat Analysis

Eight tumor habitat clusters were defined by combining binarized ADC, rCBV, and K^{trans} values using GMM. Cutoff values derived from the hist-GBM and mol-GBM were ADC = 1.326, rCBV = 4.420, and K^{trans} = 0.026. The pairwise PERMANOVA

https://doi.org/10.3348/kjr.2025.1969

Korean Journal of Radiology
KJR

showed significant differences in overall habitat distributions between hist-GBM and mol-GBM (pseudo-F = 4.45, $P = 0.003$) and between hist-GBM and mol-GBM (ext) (pseudo-F = 4.38, $P = 0.003$), but not between mol-GBM and mol-GBM (ext) (pseudo-F = 0.63, $P = 0.765$).

Median proportion (%) in cluster 0 (low ADC, low rCBV, low K^{trans}) was significantly higher in the mol-GBM (40.0% vs. 71.4%, $P < 0.001$). In contrast, the proportion of cluster 3 (low ADC, high rCBV, high K^{trans}) was significantly higher in the hist-GBM than in mol-GBM (7.0% vs. 0.8%, $P \leq 0.001$). Similarly, cluster 7 (high ADC, high rCBV, high K^{trans}) was also more prevalent in the hist-GBM (1.4% vs. 0.3%, $P = 0.036$) (Table 2). External validation using the mol-GBM (ext) dataset showed consistent results with hist-GBM in clusters 0 and 3. No significant differences were found between mol-GBM and mol-GBM (ext) across all clusters (Supplementary Table 1).

The total proportion of high-permeability habitats (high K^{trans}; clusters 1, 3, 5, and 7) was markedly higher in hist-GBM compared with mol-GBM (21.3% vs. 5.7%, $P < 0.001$). Likewise, the proportion of high-vascularity habitats (high rCBV; clusters 2, 3, 6, and 7) was significantly higher in hist-GBM (22.7% vs. 10.1%, $P = 0.001$). In contrast, no significant difference was observed in the overall proportion of high-cellularity habitats (low ADC; clusters 0, 1, 2, and 3) between the two groups (78.1% vs. 87.8%, $P = 0.163$).

The 3D habitat distributions and the corresponding 2D projections (Fig. 2, Supplementary Fig. 2) further confirmed these distinctions. Tumor volumes for clusters 3 (red; low ADC, high rCBV, high K^{trans}) and 7 (gray; high ADC, high rCBV, high K^{trans}) were greater in the hist-GBM than the in mol-GBM and mol-GBM (ext). The clustering patterns of mol-GBM and mol-GBM (ext) appeared to be identical (Fig. 2B, C), visualizing the absence of significant differences noted in Supplementary Table 1.

Representative Cases for Tumor Habitat Clustering

Representative cases (Fig. 3) illustrate these patterns. Patient A, a case of hist-GBM with marked contrast enhancement, showed a large proportion of cluster 3 (red) within the enhancing lesion. Patient B, despite minimal enhancement, also showed a marked proportion of cluster 3 in the tumor area. In contrast, patient C, a mol-GBM case with a non-enhancing lesion, showed a predominance of cluster 0 (blue; low ADC, low rCBV, low K^{trans}) within the FLAIR hyperintense region. The stacked voxel count plot (Fig. 3D) showed a higher cluster 3 proportion in hist-GBM than in mol-GBM. Moreover, high K^{trans} clusters (cluster 1, 3, 5, and 7) were more frequent in the hist-GBM (Fig. 3E). These patterns were most evident in tumors with strong contrast enhancement.

Discrimination Between Mol-GBM and Hist-GBM

Univariable logistic regression was performed to evaluate the association between habitat-derived features and the GBM subtype, the results are summarized in Supplementary Figure 3A. Features with strong univariable associations, cluster 3 proportion, high K^{trans} proportion, and Shannon

Table 2. Comparison of tumor habitat cluster proportions

Cluster	ADC	rCBV	K^{trans}	Cluster proportions (%)		*P*
				Hist-GBM (n = 39)	Mol-GBM (n = 13)	
0	↓	↓	↓	40.0 [28.9–60.1]	71.4 [64.0–79.7]	<0.001*
1	↓	↓	↑	6.1 [1.8–10.6]	3.0 [1.6–3.3]	0.059
2	↓	↑	↓	6.3 [4.7–8.6]	5.2 [3.1–7.8]	0.612
3	↓	↑	↑	7.0 [3.5–15.3]	0.8 [0.6–2.5]	<0.001*
4	↑	↓	↓	15.4 [7.2–29.6]	11.4 [5.9–16.5]	0.263
5	↑	↓	↑	1.3 [0.4–3.9]	0.4 [0.4–1.2]	0.099
6	↑	↑	↓	1.2 [0.5–2.2]	0.7 [0.4–1.6]	0.352
7	↑	↑	↑	1.4 [0.3–3.4]	0.3 [0.2–0.9]	0.036*
Composite habitat proportions						
Low ADC (clusters 0 + 1 + 2 + 3)				78.1 [54.2–87.7]	87.8 [78.6–93.7]	0.163
High rCBV (clusters 2 + 3 + 6 + 7)				22.7 [12.7–35.0]	10.1 [6.9–11.4]	0.001*
High K^{trans} (clusters 1 + 3 + 5 + 7)				21.3 [10.8–34.2]	5.7 [3.6–7.9]	<0.001*

Data are median [interquartile range].
*$P < 0.05$.
ADC = apparent diffusion coefficient, rCBV = relative cerebral blood volume, K^{trans} = volume transfer constant, Hist-GBM = histological glioblastoma, Mol-GBM = molecular glioblastoma

https://doi.org/10.3348/kjr.2025.1969

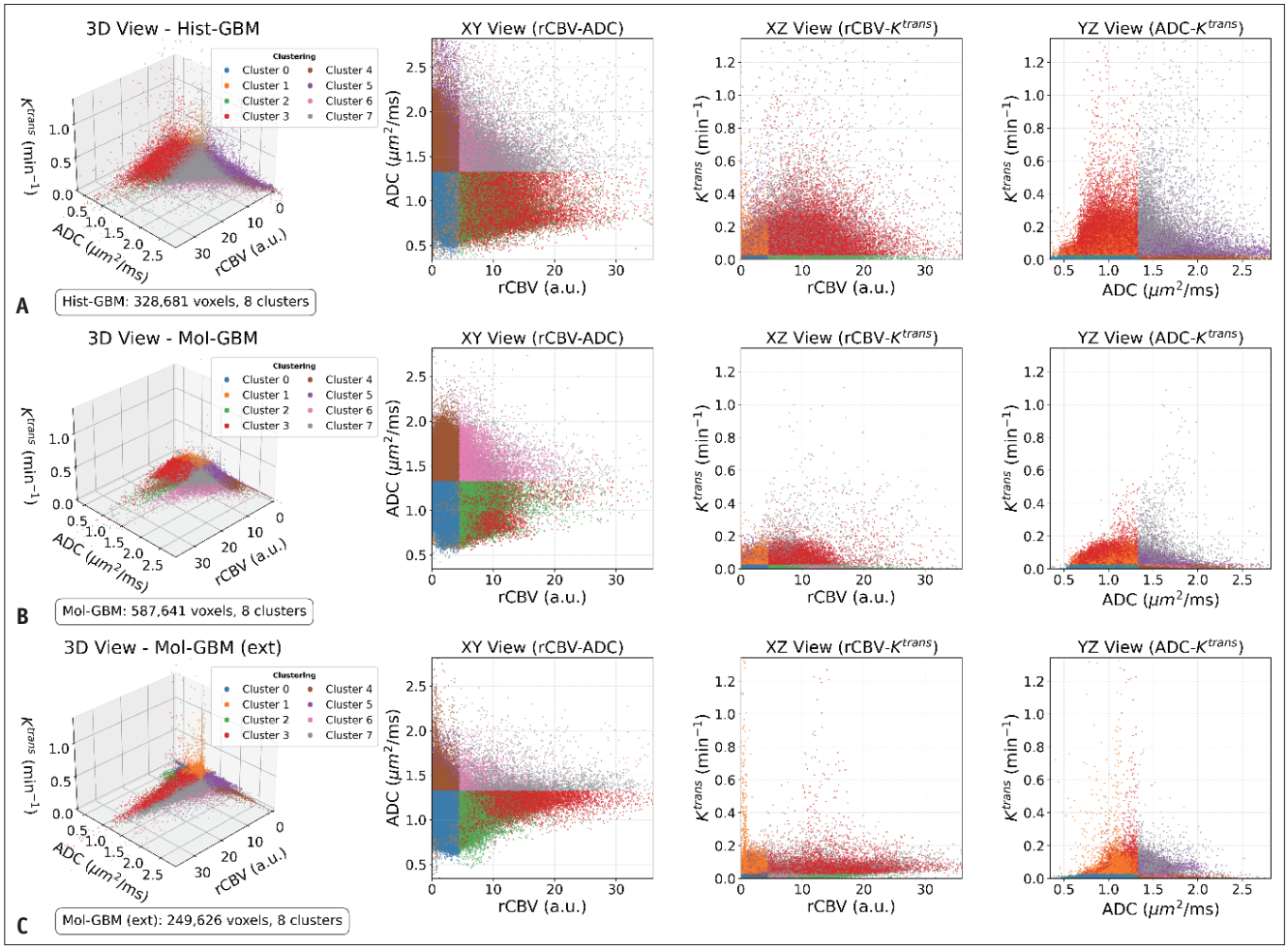

Fig. 2. Voxel-wise habitat clustering of Hist-GBM, Mol-GBM, and Mol-GBM (ext) based on multiparametric MRI. Tumor voxels were classified into eight clusters based on 2 x 2 x 2 combinations of binary high/low grouping of ADC, rCBV, and K^{trans} values using a GMM. GMM-determined cutoff values were as follows: ADC, 1.326; rCBV, 4.420; and K^{trans}, 0.026. Shown are the three-dimensional cluster distributions with their respective two-dimensional projections onto each parameter axis. **A:** Voxel data from patients in the Hist-GBM group (n = 39). For improved visualization and fair comparison, 10% of all voxels are displayed. Voxel data for Hist-GBM patients are provided in Supplementary Figure 2. **B:** Voxel data from all patients in the Mol-GBM group (n = 13). **C:** External validation of the established clustering criteria using voxel data from the Mol-GBM (ext) group (n = 9). Hist-GBM = histological glioblastoma, Mol-GBM = molecular glioblastoma, Mol-GBM (ext) = molecular glioblastoma from external dataset, ADC = apparent diffusion coefficient, rCBV = relative cerebral blood volume, K^{trans} = volume transfer constant, GMM = Gaussian mixture model

entropy, were incorporated into multivariable models as described above.

Multivariable logistic regression demonstrated that the incorporation of habitat-derived features improved discrimination compared with tumor volume alone (Fig. 4, Table 3). In the internal validation cohort, Model V achieved an AUC of 0.70 (95% CI: 0.51–0.85). Model H showed improved discrimination compared to Model V with a marginal *P*-value (AUC: 0.85, 95% CI: 0.70–0.96; *P* = 0.053). Model H+ achieved the highest AUC (0.87, 95% CI: 0.73–0.97), whereas differences from Model V and Model H were not significant (*P* = 0.057 and 0.434, respectively). Binary classification performance based on the Youden index-derived thresholds is summarized in Table 4. In the external cohort (mol-GBM only), classification accuracies were 77.8% (7/9) for Model H and 88.9% (8/9) for Model H+. As a sensitivity analysis, a multivariable model incorporating all eight habitat clusters using a centered log-ratio transformation also demonstrated robust discrimination (AUC: 0.82; Supplementary Fig. 3B), supporting the consistency of habitat-based modeling.

DISCUSSION

This study demonstrated that mol-GBM and hist-GBM

https://doi.org/10.3348/kjr.2025.1969

Korean Journal of Radiology
KJR

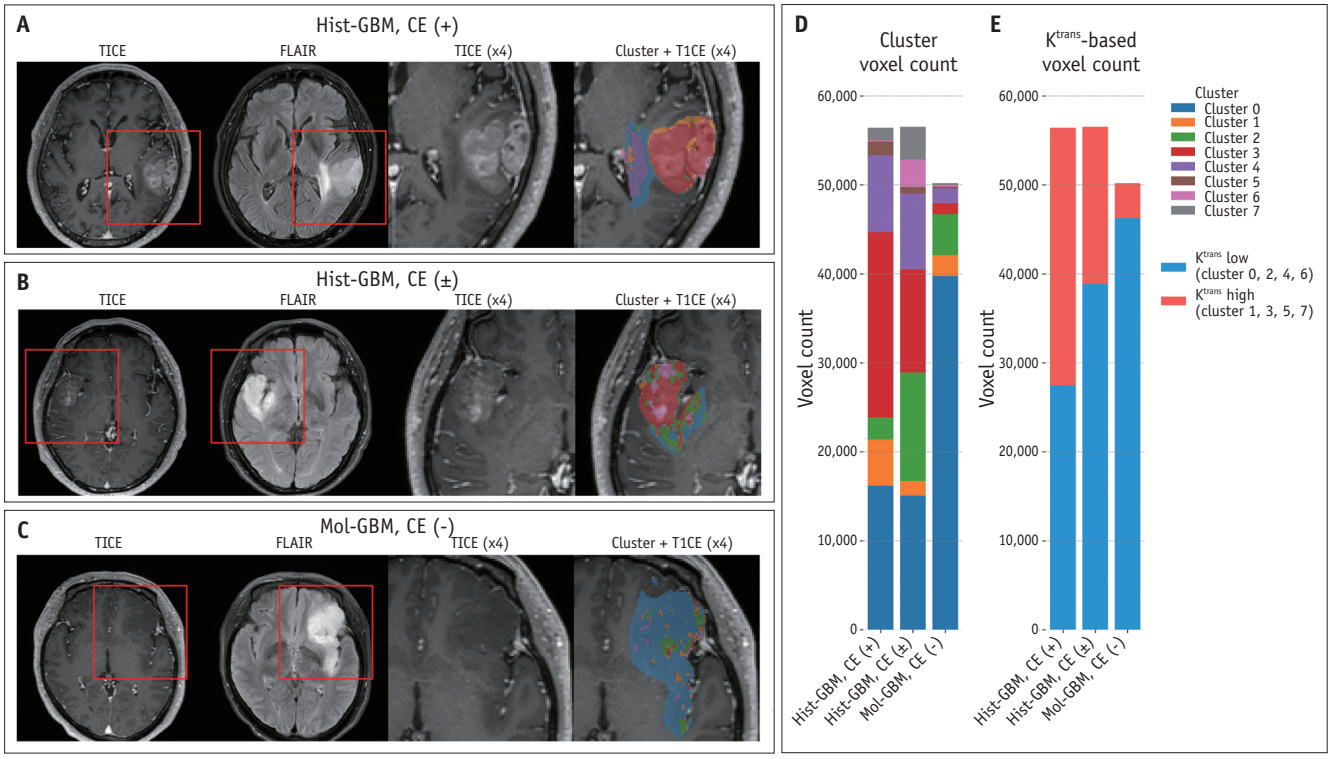

Fig. 3. Visualization of tumor clusters in Hist-GBM and Mol-GBM patients. **A-C:** Multimodal MRI of three patients with IDH-wildtype glioblastoma, presented as the T1CE image, FLAIR image, a magnified (x4) tumor region, and the corresponding cluster map overlaid on the magnified area: **(A)** Hist-GBM, CE (+); a 58-year-old male with aphasia presenting an enhancing lesion in the left temporal lobe. **(B)** Hist-GBM, CE (±); a 52-year-old female with right upper extremity paresthesia presenting a right temporal mass with minimal enhancement. **(C)** Mol-GBM, CE (-); a 56-year-old female with headache shows a non-enhancing mass in the left frontal and medial parietal lobes. **D:** Stacked bar plots demonstrate cluster-wise tumor volume distribution, highlighting increased cluster 3 volume in Hist-GBM compared with Mol-GBM. **E:** K^{trans} values were highest in the enhancing Hist-GBM, case A, followed by the minimally enhancing Hist-GBM, case B, and lowest in the non-enhancing Mol-GBM, case C. Hist-GBM = histological glioblastoma, Mol-GBM = molecular glioblastoma, IDH = isocitrate dehydrogenase, T1CE = T1-weighted contrast-enhanced, FLAIR = fluid-attenuated inversion recovery, CE = contrast enhancement, K^{trans} = volume transfer constant

differ in tumor heterogeneity using a 3D habitat analysis based on multiparametric physiologic MRI. Mol-GBM showed a smaller proportion of habitats with high vascularity and high permeability, particularly cluster 3 and high K^{trans} clusters. Hist-GBM also exhibited greater intratumoral diversity, as reflected by a higher Shannon entropy.

Prior imaging studies comparing mol-GBM and hist-GBM subtypes have relied largely on conventional MRI or global summary statistics. Although histogram metrics showed significant differences (Supplementary Table 2), such approaches overlook intratumoral heterogeneity [25]. The habitat analysis approach employed in this study overcomes this limitation. By partitioning the tumor into biologically distinct subregions based on a multiparametric physiological signature, this approach identifies localized malignant foci obscured by whole-tumor averaging [17-19]. The discovery that the most malignant-appearing habitat (cluster 3; low ADC, high rCBV, high K^{trans}) was found in hist-GBM validates the utility of this method and suggests its potential for guiding targeted biopsies toward the most aggressive tumor regions.

Although prior studies have utilized ADC (cellularity) and rCBV (vascularity), this approach has limitations, particularly in minimally enhancing tumors [17-19]. We developed this physiological characterization by incorporating K^{trans}, a quantitative parameter reflecting disruption of the blood-brain barrier and microvascular leakage [11,26-28]. Pathologically, aggressive GBM (particularly hist-GBM) is characterized by hypoxia-driven VEGF expression, which promotes the histologic hallmark of aberrant, immature neovasculature, and microvascular proliferation [29]. This immature vasculature is characterized by high permeability, which manifests as elevated K^{trans} values on DCE-MRI [30]. The significant predominance of high K^{trans} habitats in

https://doi.org/10.3348/kjr.2025.1969

hist-GBM confirms that K^{trans} sensitively captures this aggressive angiogenic activity. In multivariable analysis, high K^{trans} proportion was the only habitat feature retaining independent significance between models H and H+ (odds ratio: 2.95 and 1.90, respectively), positioning it as the key differentiator between hist-GBM and mol-GBM subtypes. Previous literature has associated "cellular, hypovascular" habitats (low ADC, low rCBV) with treatment resistance and poor prognosis, often attributed to hypoxia [17-19]. Our study refined this concept by demonstrating that this category is not monolithic. We identified two distinct clusters within the following profile: cluster 0 (low K^{trans}) and cluster 1 (high K^{trans}). Cluster 0, characterized by low permeability despite low vascularity, was significantly more prevalent in mol-GBM, whereas cluster 1 did not present low permeability. This finding suggests that hypoxic regions with concurrent high permeability may reflect true regions of active, hypoxia-driven angiogenesis and vascular leakiness [30], constituting a less aggressive and proliferative microenvironment characteristic of mol-GBM [31]. This stratification, which highlights a key biological difference between the hist-GBM and mol-GBM subtypes, was detectable only when K^{trans} was incorporated into the habitat analysis.

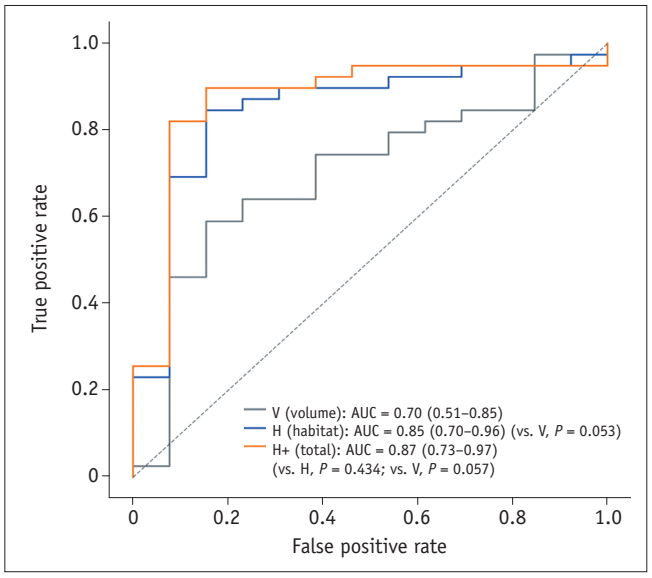

Fig. 4. Multivariable logistic regression analysis for identifying features associated with Hist-GBM versus Mol-GBM. Receiver operating characteristic curves for multivariable models predicting Hist-GBM from internal validation: Model V (volume only; AUC = 0.70 [95% CI: 0.51–0.85]), Model H (volume, cluster 3 proportion, and high K^{trans}; AUC = 0.85 [95% CI: 0.70–0.96]), and Model H+ (volume, cluster 3 proportion, high K^{trans}, and Shannon entropy; AUC = 0.87 [95% CI: 0.73–0.97]). Hist-GBM = histological glioblastoma, Mol-GBM = molecular glioblastoma, AUC = area under the curve, CI = confidence interval, K^{trans} = volume transfer constant

ADC alone provided limited discrimination. The proportion of low ADC clusters did not differ significantly between subtypes, whereas the high K^{trans} and high rCBV clusters did. ADC values are affected by not only cellularity but also by edema, necrosis, and nuclear morphology [32,33], reducing their specificity. Additionally, mol-GBM may

Table 3. Factors associated with histological glioblastoma

Variable	Model V				Model H				Model H+			
	β	aOR	95% CI	*P*	β	aOR	95% CI	*P*	β	aOR	95% CI	*P*
Tumor volume (log)	0.643	1.90	1.15–3.72	0.020	0.525	1.69	0.94–3.62	0.078	0.415	1.51	0.78–3.14	0.186
Cluster 3 proportion	-	-	-	-	0.264	1.30	0.71–2.78	0.450	0.174	1.19	0.66–2.38	0.568
High K^{trans} proportion	-	-	-	-	1.082	2.95	1.82–5.23	<0.001	0.642	1.90	1.23–3.14	0.002
Shannon entropy	-	-	-	-	-	-	-	-	0.708	2.03	1.10–4.70	0.050

β = standardized regression coefficient, aOR = adjusted odds ratio, CI = confidential interval, K^{trans} = volume transfer constant

Table 4. Binary classification performance using Youden index–derived threshold

Model	Youden threshold	Internal validation			External evaluation
		AUC (95% CI)	Mol-GBM accuracy (n = 13, %)	Hist-GBM accuracy (n = 39, %)	Mol-GBM (ext) accuracy (n = 9, %)
Model V	0.772	0.70 (0.51–0.85)	11/13 (84.6)	23/39 (59.0)	9/9 (100)*
Model H	0.612	0.85 (0.70–0.96)	11/13 (84.6)	33/39 (84.6)	7/9 (77.8)
Model H+	0.652	0.87 (0.73–0.97)	12/13 (92.3)	32/39 (82.1)	8/9 (88.9)

Decision thresholds are Youden index-derived and held fixed for external evaluation.
*The 100% external accuracy for Model V reflects its high Youden threshold (0.772), driven by the smaller tumor volumes characteristic of Mol-GBM, resulting in all 9 external cases being assigned low predicted probabilities.
Mol-GBM = molecular glioblastoma, AUC = area under the curve, CI = confidential interval, Hist-GBM = histological glioblastoma, Mol-GBM (ext) = molecular glioblastoma from external dataset

https://doi.org/10.3348/kjr.2025.1969

Korean Journal of Radiology
KJR

exhibit cellular density comparable to that of hist-GBM; Griessmair et al. [34] reported lower ADC in mol-GBM than in lower-grade astrocytoma lacking GBM-defining molecular alterations. Thus, ADC is informative but insufficient alone to distinguish mol-GBM from hist-GBM.

This study has some limitations. First, the small sample size of the mol-GBM group (n = 13 internal, n = 9 external) reflects the rarity of this entity (2.7% of IDH-wildtype GBMs in our cohort) and limits statistical power and generalizability. The findings of this exploratory study require validation in larger, prospective cohorts. Second, combining MRI data from different vendors may introduce residual batch effects despite normalization to normal white matter; future studies employing advanced harmonization techniques may further mitigate this issue. Third, the external cohort included only mol-GBM cases, limiting the evaluation of discrimination performance and generalizability. Although consistent habitat distributions were observed, external validation including both subtypes is required. Fourth, due to the retrospective study design, direct histopathological correlation of the imaging-defined habitats was not feasible. Future prospective studies integrating radiologic, histologic, and molecular data are warranted to strengthen the biological relevance and clinical applicability of these findings.

In conclusion, a 3D habitat analysis using ADC, rCBV, and K^{trans} can distinguish mol-GBM from hist-GBM subtypes by capturing differences in intratumoral heterogeneity. Mol-GBM exhibited significantly smaller tumor proportions within the most malignant habitat, and differences between two subtypes were greatest for permeability (K^{trans}). Incorporating habitat-derived features alongside tumor volume may improve discriminating the two subtypes on MRI. These findings provide novel radiologic insights into the recently classified but less-characterized mol-GBM and a provides a foundation for future radiogenomic investigations. Additional studies, including more rigorous external validation, are warranted.

Supplement

The Supplement is available with this article at https://doi.org/10.3348/kjr.2025.1969.

Availability of Data and Material

The data generated and/or analyzed during the current study are not publicly available due to patient privacy but are available from the corresponding author on reasonable request. The underlying code for this study is available in Multiparametric-MRI-Habitat-GBM and can be accessed via this link https://github.com/snuh-rad-aicon/Multiparametric-MRI-Habitat-GBM.

Conflicts of Interest

Seung Hong Choi, Deputy Editor, and Ji Eun Park, Editorial Board Member, of the *Korean Journal of Radiology*, were not involved in the editorial evaluation or decision to publish this article. The remaining authors have declared no conflicts of interest.

Author Contributions

Conceptualization: Minseo Choi, Yunseo Choi, Kyu Sung Choi. Data curation: Kyu Sung Choi. Formal analysis: Minseo Choi, Kyu Sung Choi, Junhyeok Lee, Seong Yun Jeong, Minchul Kim. Funding acquisition: Kyu Sung Choi. Investigation: Minseo Choi, Yunseo Choi, Kyu Sung Choi. Methodology: Minseo Choi, Kyu Sung Choi, Yunseo Choi, Junhyeok Lee. Project administration: Seung Hong Choi. Resources: Kyu Sung Choi, Inpyeong Hwang, Yae Won Park, Ji Eun Park. Supervision: Kyu Sung Choi, Seung Hong Choi. Validation: Kyu Sung Choi, Yae Won Park, Ji Eun Park. Visualization: Minseo Choi, Junhyeok Lee, Seong Yun Jeong. Writing—original draft: Minseo Choi. Writing—review & editing: Minseo Choi, Yunseo Choi.

ORCID IDs

Minseo Choi
https://orcid.org/0000-0001-8060-2623
Yunseo Choi
https://orcid.org/0009-0006-3606-9343
Junhyeok Lee
https://orcid.org/0000-0001-7489-5829
Seong Yun Jeong
https://orcid.org/0009-0008-3124-5437
Minchul Kim
https://orcid.org/0000-0002-4614-1146
Inpyeong Hwang
https://orcid.org/0000-0002-1291-8973
Ji Eun Park
https://orcid.org/0000-0002-4419-4682
Yae Won Park
https://orcid.org/0000-0001-8907-5401
Seung Hong Choi
https://orcid.org/0000-0002-0412-2270

Kyu Sung Choi
https://orcid.org/0000-0002-5175-3307

Funding Statement

This work was supported by the National Research Foundation of Korea (NRF) grant funded by the Korea government (MSIT) (No. RS-2023-00251022) (K.S.C.); the SNUH Research Fund (No. 04-2024-0600; No. 04-2025-2060) (K.S.C.); and the Korea Health Technology R&D Project through the Korea Health Industry Development Institute (KHIDI) grant funded by the Ministry of Health&Welfare (No. RS-2024-00439549) (K.S.C.).

Acknowledgments

We would like to thank Hyeryeon Son, RN, BSN (Department of Radiology, Seoul National University Hospital) for her invaluable assistance with data collection and analysis.

REFERENCES

1. Louis DN, Perry A, Reifenberger G, von Deimling A, Figarella-Branger D, Cavenee WK, et al. The 2016 World Health Organization classification of tumors of the central nervous system: a summary. *Acta Neuropathol* 2016;131:803-820
2. Brat DJ, Aldape K, Colman H, Holland EC, Louis DN, Jenkins RB, et al. cIMPACT-NOW update 3: recommended diagnostic criteria for "diffuse astrocytic glioma, IDH-wildtype, with molecular features of glioblastoma, WHO grade IV." *Acta Neuropathol* 2018;136:805-810
3. Ostrom QT, Bauchet L, Davis FG, Deltour I, Fisher JL, Langer CE, et al. The epidemiology of glioma in adults: a "state of the science" review. *Neuro Oncol* 2014;16:896-913
4. Ramos-Fresnedo A, Pullen MW, Perez-Vega C, Domingo RA, Akinduro OO, Almeida JP, et al. The survival outcomes of molecular glioblastoma IDH-wildtype: a multicenter study. *J Neurooncol* 2022;157:177-185
5. Ramos-Fresnedo A, Domingo RA, Perez-Vega C, Pullen MW, Akinduro OO, Almeida JP, et al. The early infiltrative phase of GBM hypothesis: are molecular glioblastomas histological glioblastomas in the making? A preliminary multicenter study. *J Neurooncol* 2022;158:497-506
6. Guo X, Gu L, Li Y, Zheng Z, Chen W, Wang Y, et al. Histological and molecular glioblastoma, IDH-wildtype: a real-world landscape using the 2021 WHO classification of central nervous system tumors. *Front Oncol* 2023;13:1200815
7. Du P, Wu X, Liu X, Chen J, Cao A, Geng D. Establishment of a prediction model based on preoperative MRI radiomics for diffuse astrocytic glioma, IDH-wildtype, with molecular features of glioblastoma. *Cancers (Basel)* 2023;15:5094
8. Foltyn-Dumitru M, Banan R, Schell M, Mahmutoglu MA, Kessler T, Wick W, et al. Histopathological and molecular characteristics of IDH-wildtype glioblastoma without contrast enhancement: implications for clinical outcomes. *Neuro Oncol* 2025;27:1878-1887
9. Sugahara T, Korogi Y, Kochi M, Ikushima I, Shigematu Y, Hirai T, et al. Usefulness of diffusion-weighted MRI with echo-planar technique in the evaluation of cellularity in gliomas. *J Magn Reson Imaging* 1999;9:53-60
10. Law M, Yang S, Babb JS, Knopp EA, Golfinos JG, Zagzag D, et al. Comparison of cerebral blood volume and vascular permeability from dynamic susceptibility contrast-enhanced perfusion MR imaging with glioma grade. *AJNR Am J Neuroradiol* 2004;25:746-755
11. Roberts HC, Roberts TP, Brasch RC, Dillon WP. Quantitative measurement of microvascular permeability in human brain tumors achieved using dynamic contrast-enhanced MR imaging: correlation with histologic grade. *AJNR Am J Neuroradiol* 2000;21:891-899
12. Yabo YA, Niclou SP, Golebiewska A. Cancer cell heterogeneity and plasticity: a paradigm shift in glioblastoma. *Neuro Oncol* 2022;24:669-682
13. Yoon J, Baek N, Yoo RE, Choi SH, Kim TM, Park CK, et al. Added value of dynamic contrast-enhanced MR imaging in deep learning-based prediction of local recurrence in grade 4 adult-type diffuse gliomas patients. *Sci Rep* 2024;14:2171
14. Martucci M, Russo R, Giordano C, Schiarelli C, D'Apolito G, Tuzza L, et al. Advanced magnetic resonance imaging in the evaluation of treated glioblastoma: a pictorial essay. *Cancers (Basel)* 2023;15:3790
15. Provenzale JM, Mukundan S, Barboriak DP. Diffusion-weighted and perfusion MR imaging for brain tumor characterization and assessment of treatment response. *Radiology* 2006;239:632-649
16. Ahn SS, Shin NY, Chang JH, Kim SH, Kim EH, Kim DW, et al. Prediction of methylguanine methyltransferase promoter methylation in glioblastoma using dynamic contrast-enhanced magnetic resonance and diffusion tensor imaging. *J Neurosurg* 2014;121:367-373
17. Moon HH, Park JE, Kim N, Park SY, Kim YH, Song SW, et al. Prospective longitudinal analysis of physiologic MRI-based tumor habitat predicts short-term patient outcomes in IDH-wildtype glioblastoma. *Neuro Oncol* 2025;27:841-853
18. Park JE, Kim HS, Kim N, Park SY, Kim YH, Kim JH. Spatiotemporal heterogeneity in multiparametric physiologic MRI is associated with patient outcomes in IDH-wildtype glioblastoma. *Clin Cancer Res* 2021;27:237-245
19. Park JE, Oh JY, Park DH, Lee HS, Yoon S, Kim N, et al. Mapping tumor habitats in isocitrate dehydrogenase -wild type glioblastoma: integrating MRI, pathologic, and RNA data from the Ivy Glioblastoma Atlas Project. *Neuro Oncol* 2025;27:291-301
20. Hoopes A, Mora JS, Dalca AV, Fischl B, Hoffmann M. SynthStrip: skull-stripping for any brain image. *Neuroimage* 2022;260:119474
21. Tustison NJ, Cook PA, Holbrook AJ, Johnson HJ, Muschelli J, Devenyi GA, et al. The ANTsX ecosystem for quantitative

biological and medical imaging. *Sci Rep* 2021;11:9068
22. van Griethuysen JJM, Fedorov A, Parmar C, Hosny A, Aucoin N, Narayan V, et al. Computational radiomics system to decode the radiographic phenotype. *Cancer Res* 2017;77:e104-e107
23. Bjornerud A, Sorensen AG, Mouridsen K, Emblem KE. T1- and T2*-dominant extravasation correction in DSC-MRI: part I—theoretical considerations and implications for assessment of tumor hemodynamic properties. *J Cereb Blood Flow Metab* 2011;31:2041-2053
24. Tofts PS, Kermode AG. Measurement of the blood-brain barrier permeability and leakage space using dynamic MR imaging. 1. Fundamental concepts. *Magn Reson Med* 1991;17:357-367
25. O'Connor JP, Rose CJ, Waterton JC, Carano RA, Parker GJ, Jackson A. Imaging intratumor heterogeneity: role in therapy response, resistance, and clinical outcome. *Clin Cancer Res* 2015;21:249-257
26. Sourbron S, Ingrisch M, Siefert A, Reiser M, Herrmann K. Quantification of cerebral blood flow, cerebral blood volume, and blood-brain-barrier leakage with DCE-MRI. *Magn Reson Med* 2009;62:205-217
27. Cuenod CA, Balvay D. Perfusion and vascular permeability: basic concepts and measurement in DCE-CT and DCE-MRI. *Diagn Interv Imaging* 2013;94:1187-1204
28. Heye AK, Culling RD, Valdés Hernández Mdel C, Thrippleton MJ, Wardlaw JM. Assessment of blood-brain barrier disruption using dynamic contrast-enhanced MRI. A systematic review. *Neuroimage Clin* 2014;6:262-274
29. Schneider SW, Ludwig T, Tatenhorst L, Braune S, Oberleithner H, Senner V, et al. Glioblastoma cells release factors that disrupt blood-brain barrier features. *Acta Neuropathol* 2004;107:272-276
30. Xue W, Du X, Wu H, Liu H, Xie T, Tong H, et al. Aberrant glioblastoma neovascularization patterns and their correlation with DCE-MRI-derived parameters following temozolomide and bevacizumab treatment. *Sci Rep* 2017;7:13894
31. Kaur B, Khwaja FW, Severson EA, Matheny SL, Brat DJ, Van Meir EG. Hypoxia and the hypoxia-inducible-factor pathway in glioma growth and angiogenesis. *Neuro Oncol* 2005;7:134-153
32. Barajas RF Jr, Phillips JJ, Parvataneni R, Molinaro A, Essock-Burns E, Bourne G, et al. Regional variation in histopathologic features of tumor specimens from treatment-naive glioblastoma correlates with anatomic and physiologic MR Imaging. *Neuro Oncol* 2012;14:942-954
33. Eidel O, Neumann JO, Burth S, Kieslich PJ, Jungk C, Sahm F, et al. Automatic analysis of cellularity in glioblastoma and correlation with ADC using trajectory analysis and automatic nuclei counting. *PLoS One* 2016;11:e0160250
34. Griessmair M, Delbridge C, Ziegenfeuter J, Jung K, Mueller T, Schramm S, et al. Exploring molecular glioblastoma: insights from advanced imaging for a nuanced understanding of the molecularly defined malignant biology. *Neurooncol Adv* 2024;6:vdae106

 https://doi.org/10.3348/kjr.2025.1969